Supporting Information

Devarakonda et al. 10.1073/pnas.1113813108

SI Text

Cloning, Protein Expression, and Purification. Estrogen-related receptor γ [ERRγ(1–120)], ERRγ(121–228), ERRγ(229–458), peroxisome proliferator activated receptor γ coactivator-1α [PGC-1α(2–220)], PGC-1α(2–150), PGC-1α(2–100), and PGC-1α(136–220) fragments were all cloned into *BamHI-XhoI* sites of either pET(kanamycin resistance) or pCDF(streptomycin resistance) vectors (Novagen) with an engineered N-terminal GST fusion tag. pcDNA3.1 (Invitrogen) ERRγ was a gift from Donald P. MacDonald (Duke University, Durham, NC). pcDNA3.1 PGC-1α WT was used as a template to generate mutants of the nuclear receptor (NR) boxes/LXXLL motifs. The QuikChange Site-Directed Mutagenesis Kit (Stratagene) was used to generate the constructs PGC-1α L1A, L2A, L3A, L2L3A (LXXLL → AXXAA and LLXXL → AAXXL), as per the manufacturer's instructions. PGC-1α(136–220) WT, PGC-1α (136–220) L2A, PGC-1α(136–220) L3A, and PGC-1α(136–220) L2L3A were all subcloned from the full-length templates into *BamHI-XhoI* sites of the pET30a-GBFusion1 vector was a gift from Gerhard Wagner (Harvard Medical school, Boston, MA), which includes a C-terminal hexahistidine tag. PGC-1α(2–220) was cloned into *NdeI-XhoI* sites of pET15b vector with an N-terminal hexahistidine tag preceding a thrombin protease cleavage site. ERRγLBD-pET15b was a gift from Dino Moras (Institut de Génétique et de Biologie Moléculaire et Cellulaire, Strasbourg, France). The GST-fusion proteins were all expressed in *Escherichia coli* BL21(DE3), induced with 1 mM isopropyl IPTG at room temperature for 4–5 h and purified using affinity chromatography on glutathione Sepharose beads using manufacturer's protocols (GE Healthcare). All the hexahistidine-tagged proteins were expressed in *E. coli* BL21(DE3), grown in terrific broth (TB) medium, induced with 1 mM IPTG at 20 °C for 12–16 h overnight. Cells were harvested, resuspended in lysis buffer (25 mM Tris, 400 mM NaCl, 20 mM imidazole, pH 7.5, 0.2 mM benzamidine, 0.2 mM PMSF, 0.1% Nonidet P-40, 10 mM b-mercaptoethanol (BME), lysed by sonication and spun at 50,000 × *g* for 30 min at 4 °C. The cleared lysate was loaded onto a preequilibrated Ni-agarose column (Qiagen) at 4 °C and the column was then washed with 50 column volumes of lysis buffer. Protein was eluted with elution buffer (25 mM Tris, 250 mM NaCl, 500 mM imidazole, 10 mM BME, pH 7.5). Protein was then concentrated using Amicon concentrators (Millipore) and purified using a S200 gel filtration column (GE Healthcare). PGC-1α(2–220) and ERRγligand binding domain (LBD) were purified separately as described, combined in excess molar ratio of ERRγLBD and subjected to thrombin (Haematologic Technologies) mediated cleavage of the hexahistidine tag. After 1 h of digestion at room temperature, the complex was loaded onto a benzamidine sepharose column (Sigma-Aldrich) to remove thrombin protease and the flow-through material was concentrated for further purification using size-exclusion chromatography.

Domain-Mapping Studies. ERRγ(1–120), ERRγ(121–228), ERRγ (229–458), PGC-1α(2–220), PGC-1α(2–150), PGC-1α(2–100), PGC-1α(136–220), PGC-1α(200–400), PGC-1α(390–470), PGC-1α (550–797) GST-fusion proteins, and GST alone were all expressed and purified as described above. pcDNA3.1 PGC-1α WT, LXXLL mutants, and ERRγ were expressed by in vitro translation using a T7 TNT Reticulocyte Lysate Kit (Promega) and radioactively labeled with ^{35}S methionine. Two micrograms of each of the GST-fusion proteins bound to glutathione sepharose beads was incubated with 5 μL of the in vitro translated labeled protein in a binding buffer containing 25 mM Tris (pH 8.0), 180 mM NaCl, 0.1% Nonidet P-40, 10 mM BME and a protease inhibitor cocktail. The binding was performed by rotating the samples at 4 °C for 2 h. The beads were then washed five times with wash buffer containing 25 mM Tris (pH 8.0), 250 mM NaCl, 0.1% Nonidet P-40, 10 mM BME, and a protease inhibitor cocktail. After all the washes, the beads were resuspended in SDS-PAGE sample buffer and electrophoresed. The gel was stained with Coomassie blue to detect the GST and fusion proteins to ensure equal loading. Radioactively labeled proteins were detected by autoradiography.

Isothermal Titration Calorimetry (ITC). ITC was used to measure thermodynamic parameters of protein-protein interactions. The experiments were performed using a VP-ITC Microcal Isothermal Titration Calorimeter (GE Healthcare). PGC-1α(136–220) WT, L2A, L3A, L2L3A and ERRγLBD were all purified as described, concentrated and prepared in a buffer suitable for ITC (50 mM Phosphate, 150 mM NaCl, 5 mM TCEP, pH 7.4). The samples were degassed for at least 10 min at 20 °C, which was the temperature at which the entire experiment was conducted. We carefully loaded 1.8 mL of 20 μM ERRγLBD into the sample cell to avoid any air bubbles. An equivalent amount of the ligand (10–20X molar excess of PGC1$\alpha^{136–220}$ WT, L2A, L3A, or L2L3A against ERRγLBD) was loaded into the injection syringe. The ligand was titrated into the sample by means of 25 individual injections via the syringe and the raw data was fitted using the software Origin 7.0 (MicroCal). The binding isotherm was fitted by a nonlinear least-squares regression using the one set of sites model. The binding Gibbs free energy (ΔG) was calculated from enthalpy changes (ΔH) and association constant (K_a) through the equation, $\Delta G = -\mathrm{RTln}\, K_a$, where R is the gas constant and T is the absolute temperature in Kelvin. The stoichiometry (n) of the interaction was determined from this fitting model.

Size-Exclusion Chromatography and Multiangle Light Scattering (SEC-MALS) (1). For determination of the Stokes radius (R_s), SEC experiments were performed with a Superdex 200 10/300 GL column (GE Healthcare) at 0.5 mL/ min at 20 °C in buffer containing 20 mM Tris·HCl (pH 7.5), 200 mM NaCl, and 5 mM DTT. The column was calibrated using the following proteins (BioRad): thyroglobulin (670 kDa, $R_s = 85$ Å), γ-globulin (158 kDa, $R_s = 52.2$ Å), ovalbumin (44 kDa, $R_s = 30.5$ Å), myoglobin (17 kDa, $R_s = 20.8$ Å), and Vitamin B12 (1,350 Da). Blue-Dextran (Sigma) was used to define the void volume of the column. Absolute molecular weights of the proteins studied were determined using MALS coupled in-line with size-exclusion chromatography. Light scattering from the column eluant was recorded at 16 different angles using a DAWN-HELEOS MALS detector (Wyatt Technology Corp.) operating at 658 nm. The detectors at different angles were calibrated using the small isotropic scatterer horse heart cytochrome C (Sigma). Protein concentration of the eluant was determined using an in-line Optilab DSP Interferometric Refractometer (Wyatt Technology Corp.). The weight-averaged molecular weight of species within defined chromatographic peaks was calculated using the ASTRA software version 5.2 (Wyatt Technology Corp.), by construction of Debye plots (KC/$R\theta$ versus $\sin^2[\theta/2]$) at 1-s data intervals. The weight-averaged molecular weight was then calculated at each point of the chromatographic trace from the Debye plot intercept and an overall average molecular weight was calculated by averaging across the peak.

Sedimentation Velocity. Sedimentation velocity ultracentrifugation experiments were performed at 25 °C with an XL A analytical ultracentrifuge (Beckman) and a TiAn60 rotor with a two-channel charcoal-filled epon centerpieces and quartz windows. Samples were analyzed at an absorbance 280 nm of approximately 1.0. Complete sedimentation velocity profiles were collected every 30 s for 50–100 boundaries at 45,000 rpm. Data were fit using the c(s) distribution model of the Lamm equation as implemented in the program SEDFIT. After optimizing meniscus position and fitting limits, the sedimentation coefficient (s) and best-fit frictional ratio (f/f_0) was determined by iterative least-squares analysis. A υ_{bar} of 0.73 cm^3/g is assumed. Solvent density ($\rho = 1.00722$ g/mL) and viscosity ($\eta = 0.010274$ poise) were derived from chemical composition by the program SEDNTERP (http://www.jphilo.mailway.com/download.htm#SEDNTERP).

Hydrogen/Deuterium Exchange (HDX) Mass Spectrometry (2). A fully automated liquid handling system (LEAP/CTC HTS PAL) manipulated protein solutions (10 μM) and diluted aliquots with a deuterium solution (of an equivalent buffer composition) for 10, 30, 60, 300, 900, and 3,600 s. Quench solution was 3 M urea, 1% TFA and peptides were eluted across a 1 mm trap and analytical column into the electrospray ionizing source of a hybrid LTQ-Orbitrap mass spectrometer (ThermoFinnigan). Data were processed with in-house developed software (3). Differential HDX values were obtained from the subtraction of the mean %D value at all time points for the apo sample, minus the mean %D value for all time points for the ligand bound sample. Samples were incubated for 2 h at room temperature prior to starting the HDX MS experiment and all data were acquired in triplicate (distinct on-exchange events, no-sample remeasurement).

Luciferase Assay. Transient transfections were performed in Ad293 cells in six well plates using Lipofectamine 2000. Cells were transfected with 100 ng estrogen-related receptor response element (ERRE) reporter construct (4), 200 ng of ERRγ, and/or 1 μg of PGC-1α WT or mutants, as indicated. Cells were harvested 20 h after transfection, luciferase activity was measured and the data were normalized to Renilla activity as an internal control.

Circular Dichroism (CD) Spectroscopy. Purified proteins were dialyzed into a buffer suitable for CD spectroscopy (15 mM Phosphate, 50 mM NaCl, 1 mM TCEP, pH 7.4). Protein concentrations for all three samples (ERRγLBD, PGC1α220, and the binary complex) were determined by measuring UV absorbance at 280 nm and using the theoretical extinction coefficients. CD spectra were measured on a J-715 Jasco spectropolarimeter from 400 μL of 1 μM protein samples in 0.2 mm path length quartz cuvettes. The spectra were an average of three accumulations, using a scanning speed of 100 nm/min, a spectral bandwidth of 1 nm, and a response time of 1 s. The experiment was repeated three times to confirm the results. The CD data were obtained on the degree ellipticity scale and converted to molar ellipticity after buffer background subtraction using the following equation:

$$\theta_{mrd} = \theta_d * M/(c * l * n_r * 10)\ [\text{deg} * \text{g/dmol} * \text{cm}^3/\text{g} * 1/\text{cm} * 1/\text{residue}],$$

where θ_d = degree ellipticity, M = molecular weight, l = path length, 10 is the dilution factor, n_r is the number of residues, and c is concentration in mg/mL. These normalized CD data were then processed using the algorithm CDFIT (http://www.ruppweb.org/cd/cdtutorial.htm#Program%20CDFIT) to calculate the percentage of secondary structural elements in each of the samples. Thermal unfolding of the three proteins was characterized by measuring the ellipticity changes at 222 nm induced by the increase in temperature of the sample from 20 to 90 °C at 5 °C/min (5–7). The JASCO spectral analysis software was used to analyze the data and to determine melting temperature associated with the unfolding of the proteins.

Fluorescence Spectroscopy. Chemical unfolding of the proteins was characterized by measuring the changes in tryptophan fluorescence induced upon titrating urea (ranging from 0 to 8 M) into protein solution. Measurements were conducted in a T-format PTI QuantaMaster C-61 spectrofluorimeter. The excitation wavelength was set to 297 nm and the emission fluorescence was acquired at 340 nm to measure tryptophan fluorescence. The intrinsic tryptophan fluorescence spectrum of 1 μM native protein was measured in a Hellma 1 cm quartz fluorescence cuvette. Pseudoequilibrium fluorescence measurements were acquired at 340 nm by titrating in 1 μM protein diluted into buffer containing 8 M urea, to gradually increase the urea concentration in the cuvette. The raw data was first adjusted for background signal from buffer. Data analysis including plotting and least-squares curve fitting using the van 't Hoff equation was done with Prism 5 (GraphPad). The midpoint of the curve, which is the concentration of denaturant (urea) where half of the protein is in unfolded state was determined.

Small-Angle X-ray Scattering (SAXS). X-ray scattering data were measured at two different synchrotron sources: beamline F2 at Cornell University High Energy Synchrotron Source (CHESS) and the SIBYLS beamline (12.3.1) at the Advanced Light Source (ALS) (8). In all cases, the forward scattering from the samples studied was recorded on a CCD detector and circularly averaged to yield one-dimensional intensity profiles as a function of Q ($Q = 4\pi \sin\theta/\lambda$, where 2θ is the scattering angle). Samples were dialyzed in 20 mM Tris·HCl (pH 7.5), 200 mM NaCl, and 5 mM DTT at 4 °C and centrifuged for 10 min at 4 °C before 0.5–30 s exposures were taken at 4 or 20 °C. Scattering from a matching buffer solution was subtracted from the data, and corrected for the incident intensity of X-rays. Replicate exposures were examined carefully for evidence of radiation damage by Guinier analysis and Kratky plot analysis. Silver behenate powder was used to locate the beam center and to calibrate the sample-to-detector distance.

SAXS at the Advanced Light Source Beamline 12.3.1 (SIBYLS). Samples were centrifuged at 3,000 rpm for 10 min at 4 °C prior to data collection. Data was collected using a 96-well plate handling sample robot, as previously described. All samples were characterized with 0.5, 1, and 6 s exposures at 20 °C, at a wavelength of 1 Å. Data were automatically reduced using custom software to provide one-dimensional intensity profiles as a function of Q (which is equal to $4\pi \sin\theta/\lambda$, where 2θ is the scattering angle). Accessible scattering was recorded in the range of $0.010 < Q < 0.35$ $Å^{-1}$.

SAXS at Cornell High Energy Synchrotron Source Beamline F2 (CHESS). Samples were centrifuged at 10,000 × *g* for 10 min at 4 °C immediately before data collection. Sample scattering profiles from beamline F2 at CHESS were collected on a custom 1,024 × 1,024 (69.78 μm) pixel CCD detector constructed by the Grüner group (Cornell University). Two-dimensional images were integrated by the BioXTAS RAW program (http://sourceforge.net/projects/bioxtasraw/) to provide one-dimensional intensity profiles as a function of Q (which is equal to $4\pi \sin\theta/\lambda$, where 2θ is the scattering angle). Measurements were taken at 4 °C via a 96-well sample-handling robot. Sample-to-detector distances of either 1,118 or 1,698 mm were used. With a calibrated wavelength of 1.26 Å (9.84 keV), scattering profiles covered a Q range from 0.012 to 0.36 $Å^{-1}$ or 0.006 to 0.27 $Å^{-1}$, respectively. Exposure

times ranged from 30 to 60 s with no attenuation, and measurements were made in triplicate unless otherwise noted.

SAXS Data Analysis. All of the preparations analyzed were monodisperse, as evidenced by linearity in the Guinier region of the scattering data and agreement of the intensity at zero [I(0)] and radius of gyration (R_g) values determined with inverse Fourier transform analysis by the programs GNOM (9). Molecular mass as derived from I(0) measurements, using the forward scatter from either bovine serum albumin or cytochrome C as a control, was consistent with the molecular masses determined by other methods. When fitting manually, the maximum diameter of the particle (D_{max}) was adjusted in 5–10 Å increments in GNOM to maximize the goodness-of-fit parameter, to minimize the discrepancy between the fit and the experimental data, and the visual qualities of the distribution profile. This analysis also yielded determinations of R_g and I(0). The theoretical SAXS profiles for atomic models were created using the CRYSOL program (10). Theoretical hydrodynamic properties on the ERRγLBD dimeric crystal structure were calculated by HYDROPRO (11).

Ensemble Optimization Method (EOM) Analysis. Structural modeling of the mixed solution conformers of PGC1α220 was performed using 2 mg/mL SAXS data over a range of $0.008 < Q < 0.30$ A^{-1} with the program EOM, which is suitable for modeling highly flexible macromolecules. In this approach, a large ensemble of randomly generated conformers (represented as bead models) is generated (12). Using a genetic algorithm, subsets of this ensemble are selected that collectively reproduce the experimental solution data and represent the different conformations assumed by the protein in solution. In this study, a pool of over 50,000 random bead conformers were generated corresponding to amino acids 2–220 of PGC-1α and their respective theoretical scatter calculated. A genetic algorithm was then implemented to identify ensembles of conformers from this pool that best agree with the data; distributions of R_g and D_{max} were calculated by the software. In Fig. 6*A*, the black curve shows the R_g and D_{max} calculated for this initial ensemble; R_g values range from 15.3 to 83.7 Å with a peak frequency at 40.3 Å, and D_{max} values extend from 41.4 to 274.4 Å with a maximum frequency near 115 Å. The red curves shown in Fig. 6*A* represent a selected ensemble of 20 conformers that combined show good concordance with the experimental SAXS data ($\chi = 1.14$). The distribution of R_g for this selected ensemble presents two distinct and equally represented populations centered at R_gs of 36 and 61 Å, respectively, as shown in Fig. 6*B*. The solution preferences of this select pool represent intrinsic properties of this protein that are not apparent from typical solution-average approaches. However, it is important to note that although the pool of structures identified represent a plausible ensemble solution that is concordant with the experimental data, it does not preclude the existence of other model ensembles that also satisfy these solution parameters.

Shape Reconstruction from SAXS Data Using DAMMIN and GASBOR. Low-resolution shapes were determined from solution scattering data using the programs DAMMIN (13) and GASBOR (14), which use different but complementary algorithms to generate shape envelopes of the scattering molecule. Bead models were visualized in PyMOL (15) or converted to meshed envelopes using SITUS (16) and visualized using UCSF Chimera (17). With GASBOR, the number of dummy residues used in shape reconstruction is prescribed by the user, requiring an understanding of the composition of the particle being modeled. Ten independent calculations were performed for each dataset using default parameters. Initially, no symmetry constraints were applied in all analyses.

In the case of ERRγLBD, calculations were then repeated assuming twofold symmetry, as justified by the apparent shape of the particle and improvement in the final χ and normalized spatial discrepancy (NSD) criterion. The models resulting from the independent runs were superimposed by the program SUPCOMB based on NSD criterion. The ten independent reconstructions were then averaged and filtered to a final consensus model using the DAMAVER suite of programs (18). Both approaches reproducibly yielded envelopes with good correlations between experimental and calculated scattering data [$\text{sqrt}(\chi) \sim 1.5$]. The ensemble of envelopes generated from multiple iterations of the reconstruction process also agreed well with one another, with NSD values ranging from 0.7 to 0.8 for DAMMIN and 1.0 to 1.3 for GASBOR (where a value of unity generally corresponds to identity between two structures, and values below one indicate a high degree of overlap). Consensus models obtained by DAMMIF and GASBOR approaches yielded similar results, unless otherwise noted.

For the binary complex, reproducible envelopes with good correlations between experimental and calculated scattering data were obtained [$\text{sqrt}(\chi) \sim 1.2$], with no symmetry restraints applied. The ensemble of envelopes generated from multiple iterations of the reconstruction process also agreed well with one another, with NSD values of 1.4 to 1.5, indicating a stable solution.

Shape Reconstruction Using MONSA. The multiphase bead modeling program MONSA (13, 19) was implemented to derive the distribution of the PGC1α220 and ERRγLBD components within the binary complex using a DAMMIN-like algorithm. In this approach, simulated annealing is employed to search for a model which simultaneously fits the data for ERRγLBD alone and the PGC1α220/ERRγLBD complex by minimization of the discrepancy between theoretical and experimental scatter. The results of multiple reconstructions were averaged by a variant DAMAVER package program SUPCOMB found at the EMBL ATSAS web site (http://www.embl-hamburg.de/biosaxs/).

Glossary of Terms.

1. Isothermal titration calorimetry (ITC). ITC is a thermodynamic technique that directly measures the heat released or absorbed when two biomolecules interact. Several thermodynamic parameters, including binding constants (K_B), reaction stoichiometry (n), enthalpy (ΔH), and entropy (ΔS), can then be derived from the measured heat. Taken together, these parameters provide a complete thermodynamic profile of the interaction between the molecules.
2. Hydrogen/deuterium exchange mass spectrometry (HDX MS). HDX MS is a study of the rate and percentage of the mass increase of a protein when the amide hydrogens are exchanged with solvent deuterium. These changes are highly dependent on local fluctuations in protein structure and are indicative of conformational mobility/stability in the regions studied. HDX studies can provide information about the dynamics of interaction between the two proteins and the effect the interaction has on local protein structure.
3. Size-exclusion chromatography in-line with multiangle light scattering (SEC-MALS). SEC-MALS combines size-exclusion chromatography with multiangle light scattering to characterize macromolecules by determining properties such as absolute mass and hydrodynamic radius, and provides a means by which protein aggregation can be quantified and the stoichiometry of macromolecular complexes determined.

i. Stokes radius (R_s). The Stokes radius or hydrodynamic radius R_H, is the radius of a hard sphere that diffuses at the same rate as the molecule and is dependent on both hydration and shape effects. For the same molecular weight, the Stokes radius varies depending on the shape of the molecule: A more extended molecule will have a larger Stokes radius compared to a more compact molecule.

4. Sedimentation velocity analytical ultracentrifugation (SV AUC). Sedimentation velocity is an analytical ultracentrifugation method that measures the rate at which molecules migrate in solution in response to an applied centrifugal force. Two parameters determined from SV experiments provide information about the shape and size of the molecules:

i. Frictional ratio (f/f_0). The frictional ratio is the ratio of the translational frictional coefficient of the molecule relative to that of a sphere of the same mass and density. Examples for commonly observed values of the hydrated frictional ratio are 1.2–1.3 for relatively globular proteins, 1.5–1.8 for asymmetric or glycosylated proteins, and larger values for very asymmetric or unfolded proteins or linear chains.
ii. Sedimentation coefficient (s). The sedimentation coefficient of a particle is defined as the ratio of a particle's sedimentation velocity to the acceleration that is applied to it (causing the sedimentation). This coefficient has the dimensions of a unit of time and is expressed in svedbergs.

5. Circular dichroism (CD) spectroscopy. CD refers to the differential absorption of left and right circularly polarized light and can be used to investigate properties of chiral molecules. CD spectroscopy is used to investigate properties of proteins in the UV range and provides spectra characteristic of the secondary structure content of the protein.
6. Fluorescence spectroscopy and intrinsic tryptophan fluorescence. Fluorescence spectroscopy analyzes fluorescence emitted from a sample upon excitation with a suitable wavelength. This method is used to study conformational changes in protein structure by analyzing intrinsic tryptophan fluorescence of the protein. Tryptophan residues are major contributors to the fluorescence signal from a protein and are typically buried in the hydrophobic core of the protein. An analysis of intrinsic fluorescence of the protein under different experimental conditions provides an assessment of the conformational changes that occur as a function of the experimental conditions.
7. Thermal and chemical denaturation. Well-ordered globular proteins show a characteristic profile upon denaturation, representing a change from a well-structured species to a completely denatured one. The dynamics of denaturation is unique to each protein and is illustrated by a melting curve. Protein unfolding can be studied either as a function of thermal denaturation or chemical denaturation (using chaotropic substances such as urea). The conformational changes that occur upon denaturation are reflected in intrinsic properties of the protein which can be studied by spectroscopic methods; changes in ellipticity at different wavelengths is representative of secondary structure content and can be analyzed by CD spectroscopy, whereas changes in intrinsic fluorescence, also illustrative of conformational changes in the protein, can be determined by fluorescence spectroscopy.
8. Small-angle X-ray scattering (SAXS). SAXS is a method that allows for the analysis of biological macromolecules in solution. When macromolecules in solution are exposed to a collimated and monochromatic X-ray beam, elastic scattering occurs. This scatter is recorded by a detector and reduced to a one-dimensional profile, plotted as intensity as a function of the scattering angle. This data can then be used to determine several structural parameters of the sample, including mass, shape, and volume. Recent innovations in analysis allow for the three-dimensional modeling of solution shape at low resolution.

i. Scattering profile. Scattering intensity from a macromolecular scattering plotted as a function of scattering angle, typically expressed as Q (where $Q = 4\pi \sin\theta/\lambda$, where 2θ is the scattering angle).
ii. Radius of gyration (R_g). The radius of gyration describes the mass distribution of the macromolecule around its center of gravity and can be derived from scattering data by two methods: Guinier analysis and the inverse Fourier transform. The Guinier approximation is obtained from the slope of the plot the natural logarithm of measured intensities versus Q^2 at the lowest scattering angles.
iii. Intensity at zero I(0). The intensity at zero scattering angle is also derived from both the Guinier approximation and the inverse Fourier transform. This value can also provide an independent estimation of the molecular mass of the macromolecule against a known standard.
iv. Inverse Fourier Transform. The inverse Fourier transform is a mathematical operation which creates a P(r) (or shape-distribution function) function from the primary scattering data. The shape-distribution plot describes the distribution of pairwise distances between all of the electrons within the macromolecular structure, plotting the probability of finding a radial distance (r) as a function of radial distance. The shape and distribution of this plot is directly correlated with a particles size and shape in solution, providing an intuitive description of a particle's solution properties.
v. D_{max}. D_{max} is the radial distance at which the value of the P(r) function returns to zero, and is indicative of the maximum intramolecular distance within the macromolecule and hence its maximum dimension.
vi. Kratky plot analysis. Kratky plot analysis displays scattering intensity as ($Q^2I(Q)$) versus the scattering vector (Q). This plot can provide a qualitative assessment of the degree of folding of a macromolecule. Well-folded macromolecules display a characteristic peak at low Q that is proportional to its molecular mass, with the profile entering a plateau at higher Q values. In contrast, increasing unfolded macromolecules show a diminution and broadening of the low Q peak feature, and the profile riles as a function of Q^2.
vii. Porod–Debye plot. Porod–Debye analysis displays scattering intensity as ($Q^4I(Q)$) versus the scattering vector (Q). This plot also is diagnostic in distinguishing the relative state of folding of a macromolecular particle.
viii. Shape/molecular envelope reconstruction. The application of the mathematics of spherical harmonics, Monte Carlo methods, and bead modeling approaches in currently available algorithms allow for the modeling of three-dimensional molecular shape at low-resolution.

9. Protein structure

i. Molten globule. A molten globule is characterized by native-like secondary structure content, but without the tightly packed protein interior and a dynamic tertiary structure. It is considered to be a thermodynamic state different both from the native (completely folded) and the denatured state (completely unfolded).
ii. Intrinsically disordered protein. Intrinsically unstructured proteins, often referred to as naturally unfolded proteins or disordered proteins, are proteins characterized by lack of stable tertiary structure when the protein exists as an isolated polypeptide chain (a subunit) under physiological conditions in vitro.
iii. Disorder-to-order transition. Disorder-to-order transition is the phenomenon in which intrinsically disordered proteins gain secondary structure and/or conformational stability upon binding to their interaction partners.
iv. Hub proteins. In protein-protein networks, a node protein which interacts with a large number of interacting partners, reaching tens and even hundreds is referred to as a hub protein.

1. Tarazona MP, Saiz E (2003) Combination of SEC/MALS experimental procedures and theoretical analysis for studying the solution properties of macromolecules. *J Biochem Biophys Methods* 56:95–116.
2. Englander JJ, Downer NW, Englander SW (1982) Reexamination of rhodopsin structure by hydrogen exchange. *J Biol Chem* 257:7982–7986.
3. Pascal BD, Chalmers MJ, Busby SA, Griffin PR (2009) HD desktop: An integrated platform for the analysis and visualization of H/D exchange data. *J Am Soc Mass Spectrom* 20:601–610.
4. Barry JB, Laganiere J, Giguere V (2006) A single nucleotide in an estrogen-related receptor alpha site can dictate mode of binding and peroxisome proliferator-activated receptor gamma coactivator 1alpha activation of target promoters. *Mol Endocrinol* 20:302–310.
5. Greenfield NJ (2006) Using circular dichroism spectra to estimate protein secondary structure. *Nat Protoc* 1:2876–2890.
6. Greenfield NJ (2006) Determination of the folding of proteins as a function of denaturants, osmolytes, or ligands using circular dichroism. *Nat Protoc* 1:2733–2741.
7. Greenfield NJ (2006) Using circular dichroism collected as a function of temperature to determine the thermodynamics of protein unfolding and binding interactions. *Nat Protoc* 1:2527–2535.
8. Hura GL, et al. (2009) Robust, high-throughput solution structural analyses by small-angle X-ray scattering (SAXS). *Nat Methods* 6:606–612.
9. Semenyuk AV, Svergun DI (1991) Gnom—a program package for small-angle scattering data-processing. *J Appl Crystallogr* 24:537–540.
10. Svergun DI, Barberato C, Koch MHJ (1995) CRYSOL—A program to evaluate X-ray solution scattering of biological macromolecules from atomic coordinates. *J Appl Crystallogr* 28:768–773.
11. Garcia De La Torre J, Huertas ML, Carrasco B (2000) Calculation of hydrodynamic properties of globular proteins from their atomic-level structure. *Biophys J* 78:719–730.
12. Bernado P, Mylonas E, Petoukhov MV, Blackledge M, Svergun DI (2007) Structural characterization of flexible proteins using small-angle X-ray scattering. *J Am Chem Soc* 129:5656–5664.
13. Svergun DI (1999) Restoring low-resolution structure of biological macromolecules from solution scattering using simulated annealing. *Biophys J* 76:2879–2886.
14. Svergun DI, Petoukhov MV, Koch MH (2001) Determination of domain structure of proteins from X-ray solution scattering. *Biophys J* 80:2946–2953.
15. DeLano WL (2002) The PyMOL Molecular Graphics System (DeLano Scientific, San Carlos, CA), Version 0.98.
16. Wriggers W, Milligan RA, McCammon JA (1998) SITUS: A package for the docking of protein crystal structures to low-resolution maps from electron microscopy. *Modeling* 16:283–283.
17. Pettersen EF, et al. (2004) UCSF Chimera–a visualization system for exploratory research and analysis. *J Comput Chem* 25:1605–1612.
18. Volkov VV, Svergun DI (2003) Uniqueness of ab initio shape determination in small-angle scattering. *J Appl Crystallogr* 36:860–864.
19. Svergun DI (1999) Restoring low-resolution structure of biological macromolecules from solution scattering using simulated annealing. *Biophys J* 77:2896–2896.

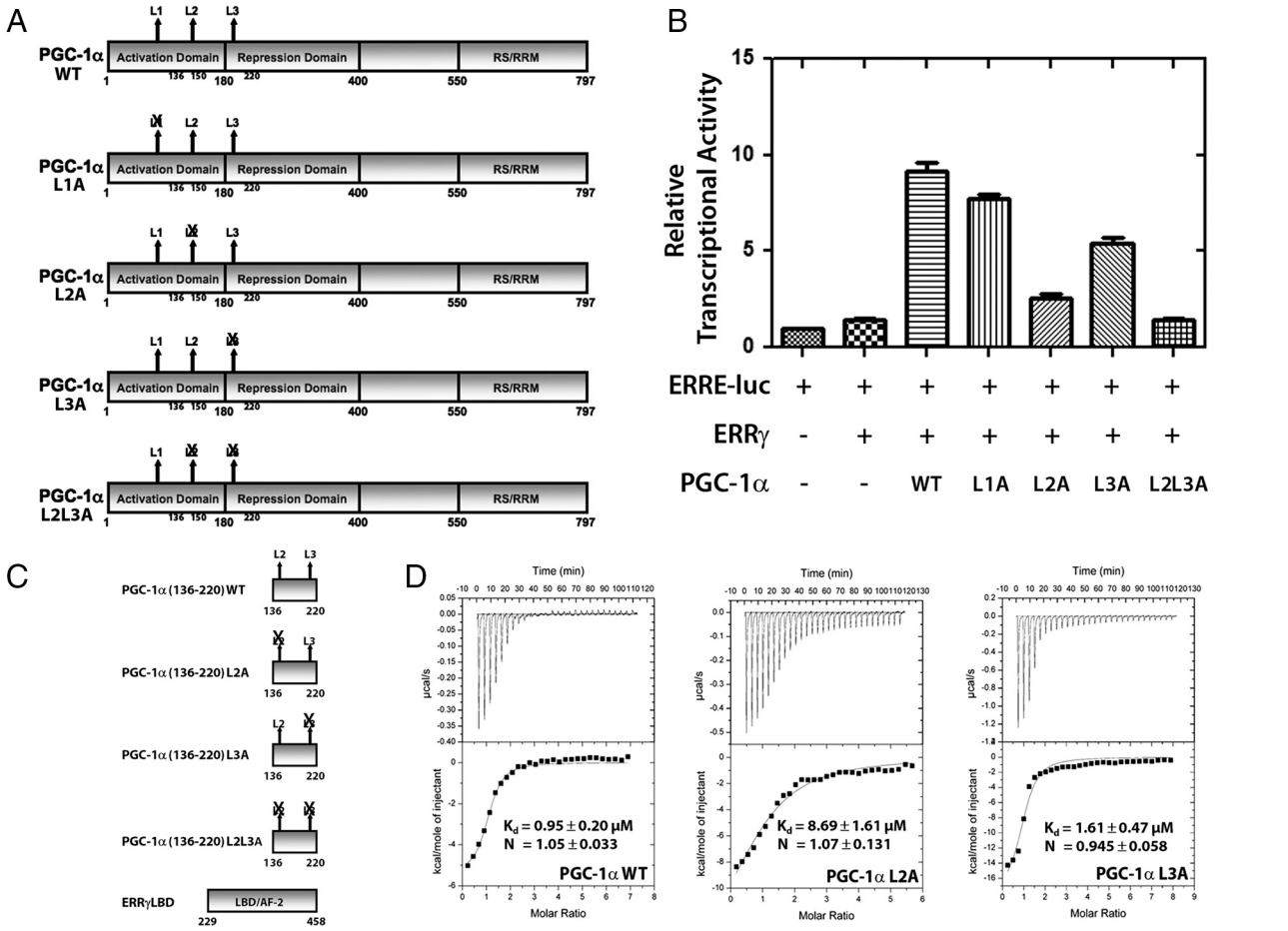

Fig. S1. Determination of the functional interaction between PGC-1α and ERRγ and relative preferences for NR boxes/LXXLL motifs. (*A*) Schematic representation of PGC-1α WT and mutants used in the assay. (*B*) Coactivation of ERRγ by PGC-1α WT and mutants from a luciferase construct consisting of ERREs tested in Ad293 cells by transiently transfecting different constructs as indicated in the figure. All data have been normalized against firefly Renilla luciferase activity. Values represented by bars are means ± standard deviation of triplicate measurements, normalized to basal ERRE luciferase activity. Data are representative of three individual experiments. Unless otherwise noted, $P < 0.01$. (*C*) Schematic representation of PGC-1α and ERRγ fragments and corresponding mutants used in the isothermal calorimetry assay. (*D*) ITC analysis of ERRγLBD against PGC-1α136-220 WT, L2A (LKKLL → AKKAA), L3A (LLKYL → AAKYL), and L2L3A. Three isotherms are shown and thermodynamic parameters are presented in Table S1 in *SI Text*.

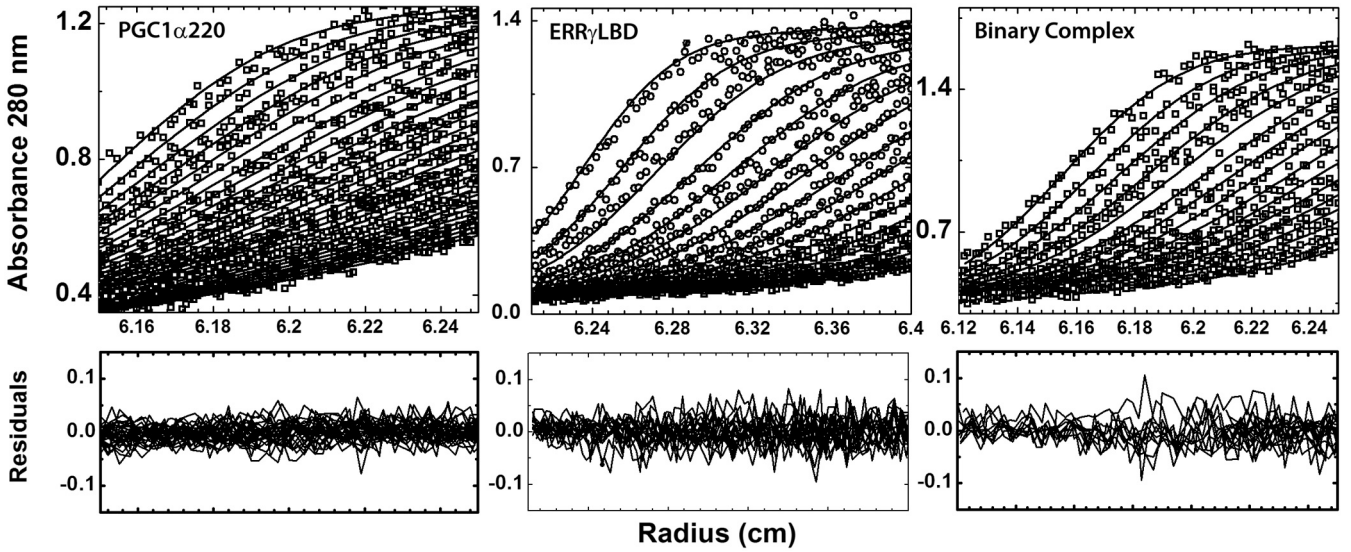

Fig. S2. Representative data from sedimentation velocity analysis. Shown from *Left* to *Right* are the experimental data for PGC1α220, ERRγLBD, and the binary complex, respectively, rendered as black points on solid black lines that are the fits to the Lamm equation. Each boundary shown corresponds to a 60-s time interval, starting at $t = 0$ (data are shown only for the initial boundaries of this analysis). Residuals, showing the agreement between the absorbance data collected and the theoretical fit to the Lamm equation, are shown below each panel as a function of the radius of the experimental cell.

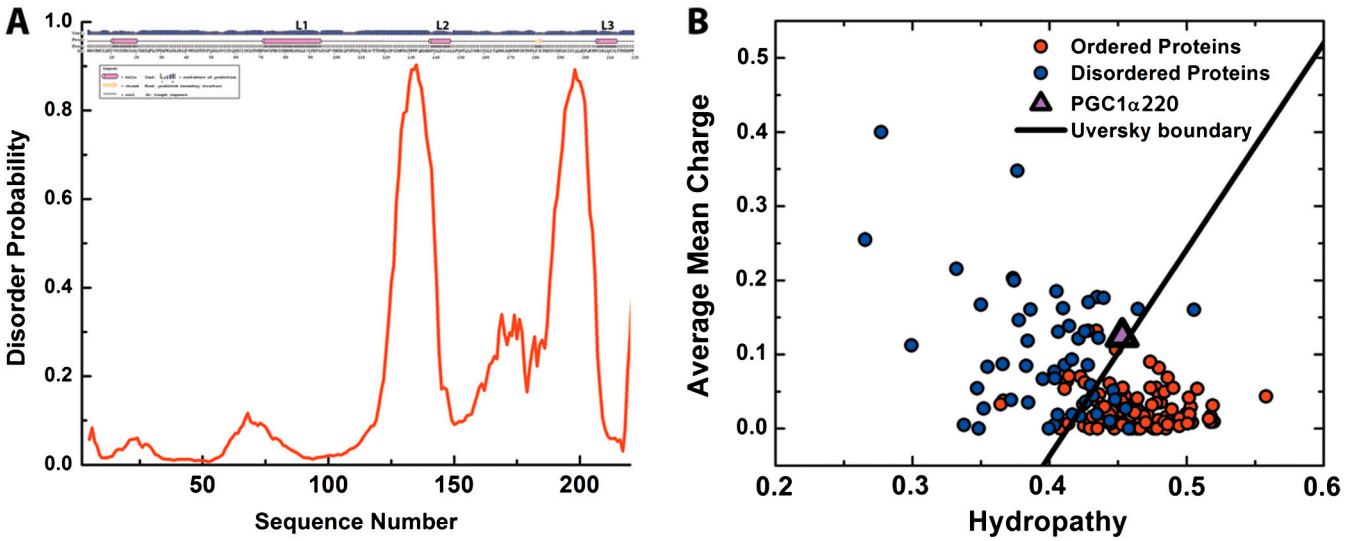

Fig. S3. Bioinformatic analysis of PGC1α220. (*A*, *Top*) Amino acid sequence-based secondary structure prediction was performed using the PSIPRED protein structure prediction server (http://bioinf.cs.ucl.ac.uk/psipred/). The predicted secondary structure elements are shown as pink cylinders (helices) or yellow arrows (beta sheets). The three NR boxes/LXXLL motifs are indicated as L1, L2, and L3. (*Bottom*) Amino acid sequence-based prediction of disorder probability was performed using the algorithm DISOPRED2 (1). The prediction indicates that the C-terminal region of the activation domain consisting of two of the three LXXLL motifs is highly disordered. The more ordered N-terminal region of the domain (aa 1–100) contains binding sites for chromatin modifying complex such as CREB binding protein/p300 and steroid receptor coactivator-1 and is important for the transcriptional activity of PGC-1α. (*B*) Hydropathy analysis of PGC1α220 amino acid sequence based on the normalized net charge versus mean hydrophobicity in comparison to that of two sets of proteins: small globular folded proteins and natively unfolded proteins (2). The plot shows the segregation between stably folded and natively unfolded proteins based on their localization within the charge-hydrophobicity phase shape. PGC1α220 is characterized by a combination of low overall hydrophobicity and large net charge and conforms to the characterization thus described. However, large-scale analyses performed by Price et al. (3) primarily on bacterial proteins, provide experimental evidence for deviations from this theory. The data suggests that classification of proteins into either stably folded or natively unfolded proteins as predicted by the Uversky plot can only be established definitively with further experimental evidence.

1 Ward JJ, Sodhi JS, McGuffin LJ, Buxton BF, Jones DT (2004) Prediction and functional analysis of native disorder in proteins from the three kingdoms of life. *J Mol Biol* 337:635–645.
2 Price WN, II, et al. (2009) Understanding the physical properties that control protein crystallization by analysis of large-scale experimental data. *Nat Biotechnol* 27:51–57.
3 Uversky VN, Gillespie JR, Fink AL (2000) Why are "natively unfolded" proteins unstructured under physiologic conditions? *Proteins* 41:415–427.

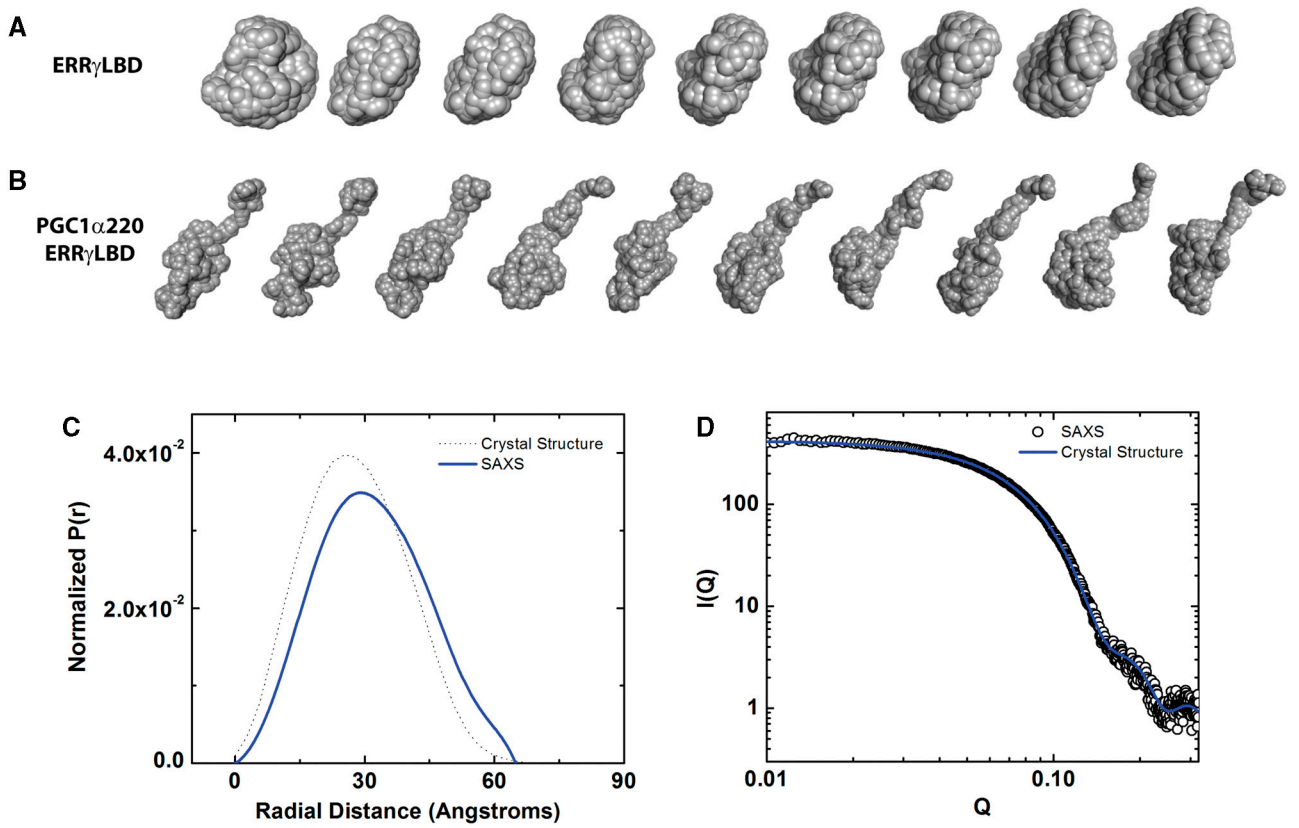

Fig. S4. Shape reconstruction from SAXS data and comparison with ERRγLBD crystal structure. Representative gallery of models from shape reconstruction performed using GASBOR for (*A*) ERRγLBD and (*B*) PGC1α220–ERRγLBD binary complex. (*C*) Comparison of the experimental shape-distribution function with theoretical profile for ERRγLBD (PDB ID code 1KV6). (*D*) CRYSOL analysis of the experimental scattering profile against the available crystal structure.

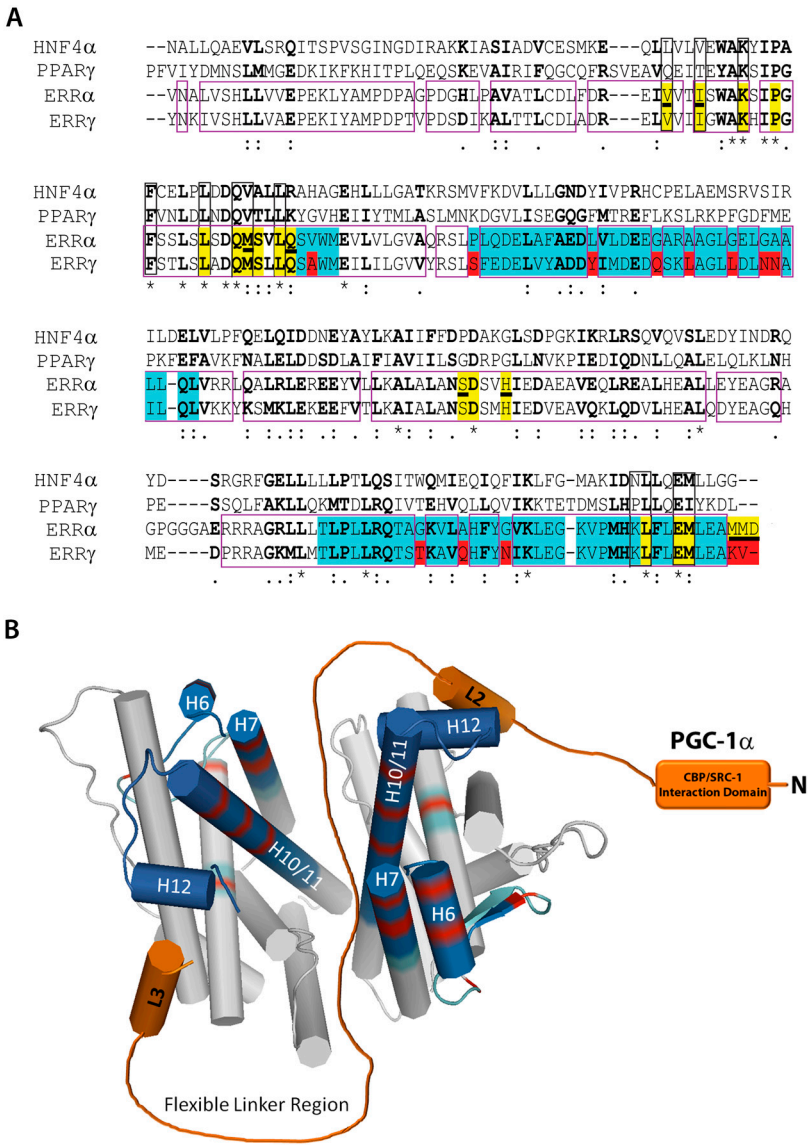

Fig. S5. Sequence alignment of HNF4α, peroxisome proliferator-activated receptor (PPAR) γ, ERRα, and ERRγLBDs and comparison of coactivator interacting regions of ERRα and ERRγ. (*A*) Sequence alignment of nuclear receptor LBDs whose crystal structures in complex with the PGC-1α LXXLL motifs have been solved, in comparison to the ERRγLBD sequence. Bold letters indicate residues conserved between all four sequences with the extent of conservation indicated at the bottom of the alignment. Black boxes indicate LBD residues that make contact with the LXXLL region as indicated by the crystal structures. These residues are highly conserved between all the LBDs. Purple boxes indicate residues that are conserved between ERRα and ERRγ, indicating a high degree of similarity between the two isoforms. Yellow highlight indicates residues in ERRα important for LXXLL recognition through direct or indirect interactions. Subset of these residues unique to ERRα have been underlined; these residues contribute to specificity of ERRα interaction with PGC-1α and are mostly conserved between ERRα and ERRγ (also highlighted in yellow) except for the last three residues. Presumably, these residues also confer specificity for the ERRγ/PGC-1α interaction. Blue highlight indicates residues in ERRγ involved in interaction with PGC-1α based on HDX analysis. Red highlight indicates residues located within the coactivator interaction region in ERRγ which distinguish it from ERRα. (*B*) Residues within the PGC-1α interaction regions of ERRγLBD unique to ERRγ vis-à-vis ERRα are mapped onto the predicted structural model for the binary complex and are indicated in red. Based on our model, we predict that mutation of residues located in helices 10/11 and 12 (Thr^{429}, Gln, Asn^{437}, $LysA^{457}$, Val^{458}) will have a significant effect on coactivator interaction interface and stoichiometry. Residues Ala^{304}, Ser^{319}, Tyr^{330}, Gln^{336}, Leu^{339}, Asn^{346}, and Asn^{347}, which are located in the coactivator interacting regions of the LBD are not conserved between ERRγ and ERRα and could potentially play an important role in establishing specificity.

Table S1. Thermodynamic parameters of the molecular interactions between ERRγLBD and WT or the LXXLL mutants of PGC-1$\alpha^{136–220}$ measured by ITC

ERRγLBD ligand	K_d (μM)	ΔH (Cal/mol)	−TΔS (Cal/mol)	N*
PGC-1$\alpha^{136–220}$ WT	0.95 ± 0.20	−5410 ± 226.3	−2695.6	1.05 ± 0.033
PGC-1$\alpha^{136–220}$ L2A	8.69 ± 1.61	−16450 ± 2505	9610.4	1.07 ± 0.131
PGC-1$\alpha^{136–220}$ L3A	1.61 ± 0.47	−18130 ± 1462	10284.3	0.945 ± 0.058
PGC-1$\alpha^{136–220}$ L2L3A	No binding	N/A	N/A	N/A

Data were determined at 20 °C and at pH 7.5 as described in *Materials and Methods*. The reported values contain some degree of errors indicated by the standard deviation. N/A, not applicable.

*The apparent stoichiometry for homodimer binding to the coactivator peptide from the curve fitting data is shown.

Table S2. Table for HDX kinetics data for PGC1α220 alone

Sequence	z	Start	End	Average	%D	SD (%)	10 s (%)	30 s (%)	60 s (%)	300 s (%)	900 s (%)	3,600 s (%)
GSSHHHHHHSSGLVPR	3	2	17	42	1	43	43	43	43	40	40	
SSHHHHHHSSGLVPR	2	3	17	45	1	47	48	46	46	41	41	
HHSSGLVPR	3	9	17	80	2	83	89	80	79	77	72	
DMCSQD	1	23	28	81	1	88	85	84	80	76	73	
SDIECA	1	32	37	115	14	103	102	128	122	104	129	
ALVGEDQPLCPDL	1	38	50	53	1	55	56	57	52	50	46	
ALVGEDQPLCPDL	2	38	50	51	1	55	51	54	51	46	46	
ALVGEDQPLCPDLPEL	2	38	53	90	1	91	94	91	89	90	83	
VGEDQPLC	1	40	47	89	2	92	93	93	90	83	82	
VGEDQPLCPDL	1	40	50	79	1	82	81	82	79	75	77	
VGEDQPLCPDL	2	40	50	86	1	92	90	92	85	83	76	
VGEDQPLCPDLPEL	1	40	53	77	1	80	80	79	76	73	73	
VGEDQPLCPDLPEL	2	40	53	88	1	92	91	91	88	84	82	
VGEDQPLCPDLPELD	2	40	54	82	1	85	85	85	82	77	78	
VGEDQPLCPDLPELDLSE	2	40	57	85	2	87	89	85	86	81	82	
PDLPELDL	1	48	55	119	1	125	124	127	117	113	110	
PDLPELDL	2	48	55	99	2	102	101	105	105	94	87	
PELDL	1	51	55	153	5	164	146	163	155	151	140	
LDVNDL	1	58	63	104	2	108	112	106	99	100	98	
LDVNDLDTDS	1	58	67	78	2	82	81	82	77	74	73	
LDVNDLDTDSF	1	58	68	73	1	76	75	75	73	70	69	
LDVNDLDTDSF	2	58	68	83	1	87	86	85	82	79	77	
LDVNDLDTDSFLGGLKWCSDQSE	2	58	80	87	1	90	90	87	86	88	82	
DVNDLDTDS	1	59	67	74	2	79	78	70	75	73	71	
DVNDLDTDSF	1	59	68	77	1	80	80	79	77	74	71	
DVNDLDTDSFL	1	59	69	73	1	76	75	75	74	70	69	
DVNDLDTDSFL	2	59	69	82	1	86	86	85	81	78	76	
DVNDLDTDSFLGGLK	2	59	73	90	1	92	91	91	91	88	88	
DVNDLDTDSFLGGLKWCSDQSE	2	59	80	87	2	87	95	88	89	80	85	
DVNDLDTDSFLGGLKWCSDQSE	3	59	80	89	1	93	91	92	90	85	83	
LDTDSFLGGLKWCSDQSE	2	63	80	98	2	99	101	98	99	96	93	
DTDSFL	1	64	69	92	2	97	99	93	90	88	86	
DTDSFLGGLK	2	64	73	99	2	99	106	104	97	94	94	
DSFLGGLKWCSDQSE	2	66	80	106	3	106	104	112	105	109	98	
FLGGLK	2	68	73	90	3	98	94	87	88	87	84	
FLGGLKWCSD	2	68	77	96	1	101	99	101	94	92	89	
FLGGLKWCSDQ	2	68	78	55	1	43	52	52	59	60	65	
FLGGLKWCSDQS	2	68	79	88	1	93	90	89	90	85	81	
FLGGLKWCSDQSE	2	68	80	88	3	95	84	93	87	86	82	
LGGLKW	2	69	74	102	4	109	105	104	104	94	94	
LGGLKWC	2	69	75	109	2	109	115	111	108	107	105	
LGGLKWCSD	2	69	77	96	1	101	98	102	94	92	88	
LGGLKWCSDQ	2	69	78	103%	2	107	104	105	101	101	100	
LGGLKWCSDQS	2	69	79	98	6	101	101	96	89	91	109	
LGGLKWCSDQSE	1	69	80	77	1	80	80	81	77	71	71	
LGGLKWCSDQSE	2	69	80	94	1	99	98	98	94	89	87	
GGLKWCSDQSE	2	70	80	98	1	104	103	102	98	93%	91	
QSEIISNQYNNEPANI	2	78	93	96	1	99	100	98	95	92	89	

Sequence	z	Start	End	Average	%D	SD (%)	10 s (%)	30 s (%)	60 s (%)	300 s (%)	900 s (%)	3,600 s (%)
SEIISNQYNNEPANIF	2	79	94	102	2	101	104	104	99	103	103	
EIISNQYNNEPANI	2	80	93	99	1	103	104	101	98	96	93	
EIISNQYNNEPANIF	2	80	94	100	1	104	102	103	98	97	94	
IISNQYNNEPAN	1	81	92	84	2	87	88	92	83	79	77	
IISNQYNNEPAN	2	81	92	101	2	106	105	102	101	97	95	
IISNQYNNEPANI	1	81	93	84	1	87	87	86	84	79	79	
IISNQYNNEPANI	2	81	93	101	1	105	105	104	102	97	95	
IISNQYNNEPANIF	1	81	94	107	1	111	109	113	106	103	100	
IISNQYNNEPANIFE	2	81	95	100	1	104	103	104	100	98	93	
IISNQYNNEPANIFEKIDEENEANLL	3	81	106	109	1	112	112	114	108	106	103	
ISNQYNNEPANIF	2	82	94	92	0	95	95	95	91	89	87	
IFEKIDEENEANL	2	93	105	98	1	102	101	100	99	93	92	
FEKIDEE	2	94	100	100	1	99	105	104	99	93	99	
FEKIDEENE	2	94	102	96	8	99	108	86	101	89	91	
FEKIDEENEAN	2	94	104	94	2	97	94	93	95	94	89	
FEKIDEENEANL	1	94	105	82	1	84	84	88	81	77	75	
FEKIDEENEANL	2	94	105	99	1	102	103	103	100	95	93	
FEKIDEENEANLL	1	94	106	82	1	84	85	89	82	76	76	
FEKIDEENEANLL	2	94	106	96	1	99	98	101	95	92	90	
EKIDEENE	2	95	102	104	1	107	106	110	104	101	95	
EKIDEENEANL	1	95	105	83	2	85	87	85	82	77	81	
EKIDEENEANL	2	95	105	101	2	104	107	104	102	97	94	
EKIDEENEANLL	1	95	106	83	1	87	86	89	86	76	75	
EKIDEENEANLL	2	95	106	95	1	98	98	98	95	90	90	
KIDEENEANL	1	96	105	79	1	82	83	81	80	75	74	
KIDEENEANL	2	96	105	95	1	99	98	99	95	90	88	
KIDEENEANLL	1	96	106	77	1	79	80	81	78	76	70	
KIDEENEANLL	2	96	106	82	1	88	85	89	80	79	74	
LDSLPVDEDGLPSF	2	113	126	122	6	126	125	121	125	114	125	
DSLPVDE	1	114	120	82	2	86	86	84	82	78	75%	
DSLPVDEDGL	1	114	123	78	1	82	80	84	77	74	74	
DSLPVDEDGLPSF	1	114	126	80	1	85	83	83	81	77	73	
DSLPVDEDGLPSF	2	114	126	87	1	91	89	90	87	83	79	
DSLPVDEDGLPSFD	1	114	127	75	3	75	77	82	74	75	69	
SLPVDEDGLP	1	115	124	109	1	112	112	111	108	108	104	
PVDEDGLPSF	1	117	126	84	2	88	85	86	85	81	80	
PVDEDGLPSF	2	117	126	95	5	98	97	96	94	90	94	
DALTDGA	1	127	133	81	1	83	84	84	81	77	76	
DALTDGAVTTDN	1	127	138	94	1	100	96	98	94	90	88	
DALTDGAVTTDN	2	127	138	129	2	136	126	139	125	126	122	
DALTDGAVTTDNE	2	127	139	78	1	81	81	82	77	74	73	
DALTDGAVTTDNEASPSSMPDGTPPPQE	2	127	154	101	1	105	103	104	100	97	93	
DALTDGAVTTDNEASPSSMPDGTPPPQE	3	127	154	95	1	99	97	99	96	92	89	
DALTDGAVTTDNEASPSSMPDGTPPPQEAEE	2	127	157	99	1	104	102	103	99	96	93	
DALTDGAVTTDNEASPSSMPDGTPPPQEAEEPSL	3	127	160	99	2	105	105	105	99	93	87	
DALTDGAVTTDNEASPSSMPDGTPPPQE AEEPSLLKKLLLAPANTQL	3	127	173	104	2	108	108	109	103	101	94	
AVTTDNEASPSSMPDGTPPPQE	2	133	154	93	1	97	95	97	92	89	86	
AEEPSL	1	155	160	112	2	117	116	115	111	109	104	
AEEPSLLKKLLL	2	155	166	120	4	123	124	124	116	125	109	
AEEPSLLKKLLL	3	155	166	108	1	112	114	113	107	103	99%	
PSLLKKLLLAPANTQL	2	158	173	107	2	111	108	114	107	103	100	
PSLLKKLLLAPANTQL	3	158	173	121	2	124	124	130	116	120	111	
LKKLLLAPA	2	161	169	109	2	111	112	112	108	102	107	
LKKLLLAPAN	2	161	170	107	2	111	111	111	105	106	95	
LKKLLLAPANTQ	2	161	172	110	1	115	115	115	109	104	103	
LKKLLLAPANTQL	1	161	173	92	1	96	95	95	93	87	86	
LKKLLLAPANTQL	2	161	173	111	1	115	114	115	111	108	104	
LKKLLLAPANTQL	3	161	173	113	1	118	117	118	112	109	105	
LKKLLLAPANTQLS	2	161	174	106	1	109	110	111	105	102	98	
LKKLLLAPANTQLS	3	161	174	112	1	118	115	119	111	109	103	
LKKLLLAPANTQLSY	2	161	175	105	1	109	108	108	104	100	97	
LKKLLLAPANTQLSY	3	161	175	114	1	117	117	117	113	110	106	
KKLLLAPANTQL	2	162	173	111	1	116	115	114	111	107	104	
LLLAPANTQL	2	164	173	108	1	114	112	113	107	104	100	
LAPANTQL	2	166	173	113	2	118	117	114	117	110	105	
SYNECSG	1	174	180	87	1	90	90	92	89	83	80	
SYNECSGL	2	174	181	92	4	99	91	105	87	90	79	
SYNECSGLSTQNHAANHTHRIRTNPAI	3	174	200	72	4	73	72	85	69	67	65	
LLKYLTTND	2	228	236	105	1	111	107	111	104	101	98	
LKYLTTND	1	229	236	97	1	101	101	99	98	92	90	
LKYLTTND	2	229	236	112	1	117	116	116	112	108	104	
LTTND	1	232	236	132	11	130	157	138	119	118	128	

Table S3. Table of structural parameters derived from SAXS analysis

Sample	Conc by I(0)	qR_g	Rg (Å)	$I(0)$	Q	R_g (Å)	$I(0)$	D_{max} (Å)
		Guinier			GNOM			
	mg/mL							
ALS SIBYLS								
PGC1α220	4.5	0.608–1.1.01	60.6 ± 2.74	171.16 ± 4.08	0.011–0.32	59.0	164	240
	2.5	0.615–1.29	61.3 ± 1.86	101.92 ± 2.53	0.011–0.322	64.5	101	220
CHESS F2								
ERRγLBD	11.5	0.459–1.43	28.7 ± 0.10	84.20 ± 0.23	0.016–0.21	27.7	82.2	80
	8.9	0.442–1.38	27.7 ± 0.13	65.37 ± 0.22	0.015–0.21	26.8	64.1	75
ALS SIBYLS								
ERRγLBD	5.7	0.259–1.22	25.8 ± 0.048	435.15 ± 0.479	0.011–0.25	26.1	425	95
	3.4	0.254–1.19	25.3 ± 0.070	260.08 ± 0.417	0.011–0.22	25.1	259	82
	2.1	0.255–1.20	25.4 ± 0.104	158.11 ± 0.381	0.011–0.26	25.2	157	95
	1.6	0.257–1.21	25.6 ± 0.126	124.06 ± 0.366	0.011–0.26	25.4	123	85
	inf. dil.	0.254–1.21	25.3 ± 0.04	—	—	25.1	—	90
ALS SIBYLS								
PGC1α220—ERRγLBD	5.6	0.450–1.24	44.9 ± 0.162	625.85 ± 1.61	0.011–0.20	49.7	643	195
	2.8	0.455–1.26	45.4 ± 0.243	313.11 ± 1.24	0.011–0.20	50.3	322	190
	1.7	0.461–1.27	45.9 ± 0.394	187.58 ± 1.20	0.011–0.20	51.6	194	195
	1.2	0.425–1.17	42.4 ± 0.535	134.00 ± 1.10	0.011–0.20	45.4	135	170
	inf. dil	0.425–1.09	42.3 ± 0.225	—	—	44.7	—	175

Table S4. Table for differential HDX data for PGC1α220 +/− ERRγLBD

Sequence	z	Start	End	Change (%)	Standard
GSSHHHHHHSSGLVPR	3	2	17	2	2
SSHHHHHHSSGLVPR	2	3	17	1	2
HHSSGLVPR	3	9	17	2	3
DMCSQD	1	23	28	1	2
ALVGEDQPLCPDL	1	38	50	−1	2
ALVGEDQPLCPDL	2	38	50	−1	1
ALVGEDQPLCPDLPEL	2	38	53	1	2
VGEDQPLC	1	40	47	3	2
VGEDQPLCPDL	1	40	50	−1	1
VGEDQPLCPDL	2	40	50	0	2
VGEDQPLCPDLPEL	1	40	53	1	2
VGEDQPLCPDLPEL	2	40	53	−1	1
VGEDQPLCPDLPELD	2	40	54	−1	2
VGEDQPLCPDLPELDLSE	2	40	57	−1	3
PDLPELDL	1	48	55	−2	2
PELDL	1	51	55	2	5
LDVNDL	1	58	63	−1	3
LDVNDLDTDS	1	58	67	1	2
LDVNDLDTDSF	1	58	68	0	1
LDVNDLDTDSF	2	58	68	−1	1
LDVNDLDTDSFLGGLKWCSDQSE	2	58	80	0	2
DVNDLDTDS	1	59	67	1	3
DVNDLDTDSF	1	59	68	0	1
DVNDLDTDSFL	1	59	69	0	1
DVNDLDTDSFL	2	59	69	−1	2
DVNDLDTDSFLGGLK	2	59	73	3	2
DVNDLDTDSFLGGLKWCSDQSE	2	59	80	−2	4
DVNDLDTDSFLGGLKWCSDQSE	3	59	80	0	1
LDTDSFLGGLKWCSDQSE	2	63	80	−4	2
DTDSFL	1	64	69	−2	3
DSFLGGLKWCSDQSE	2	66	80	−3	4
FLGGLK	2	68	73	1	5
FLGGLKWCSD	2	68	77	1	1
FLGGLKWCSDQ	2	68	78	1	1
FLGGLKWCSDQS	2	68	79	−3	2
FLGGLKWCSDQSE	2	68	80	−3	4
LGGLKWCSD	2	69	77	0	2
LGGLKWCSDQ	2	69	78	-2	3
LGGLKWCSDQS	2	69	79	−5	7
LGGLKWCSDQSE	1	69	80	0	1
LGGLKWCSDQSE	2	69	80	0	1
GGLKWCSDQSE	2	70	80	0	2
SEIISNQYNNEPANIF	2	79	94	0	3
EIISNQYNNEPANIF	2	80	94	0	1

Sequence	z	Start	End	Change (%)	Standard
IISNQYNNEPAN	1	81	92	−1	2
IISNQYNNEPAN	2	81	92	0	2
IISNQYNNEPANI	1	81	93	2	2
IISNQYNNEPANI	2	81	93	0	2
IISNQYNNEPANIF	1	81	94	0	2
IISNQYNNEPANIFE	2	81	95	0	1
IISNQYNNEPANIFEKIDEENEANLL	3	81	106	0	2
ISNQYNNEPANIF	2	82	94	−1	0
IFEKIDEENEANL	2	93	105	1	2
FEKIDEENE	2	94	102	−3	11
FEKIDEENEAN	2	94	104	−1	3
FEKIDEENEANL	1	94	105	2	2
FEKIDEENEANL	2	94	105	1	2
FEKIDEENEANLL	1	94	106	0	1
FEKIDEENEANLL	2	94	106	1	1
EKIDEENEANL	1	95	105	0	2
EKIDEENEANL	2	95	105	1	2
EKIDEENEANLL	1	95	106	2	2
EKIDEENEANLL	2	95	106	0	2
KIDEENEANL	1	96	105	1	1
KIDEENEANL	2	96	105	−1	2
KIDEENEANLL	1	96	106	1	2
KIDEENEANLL	2	96	106	−2	2
TLDSLPVDEDGLPSF	2	112	126	−1	1
LDSLPVDEDGLPSF	2	113	126	0	8
DSLPVDE	1	114	120	0	2
DSLPVDEDGL	1	114	123	1	2
DSLPVDEDGLPSF	1	114	126	1	2
DSLPVDEDGLPSF	2	114	126	0	1
DSLPVDEDGLPSFD	1	114	127	1	4
SLPVDEDGLP	1	115	124	-1	2
PVDEDGLPSF	1	117	126	0	2
PVDEDGLPSF	2	117	126	−1	5
DALTDGA	1	127	133	6	1
DALTDGAVTTD	1	127	137	0	1
DALTDGAVTTDN	1	127	138	−1	2
DALTDGAVTTDNE	2	127	139	2	1
DALTDGAVTTDNEASPSSMPDGTPPPQE	2	127	154	0	1
DALTDGAVTTDNEASPSSMPDGTPPPQE	3	127	154	2	1
DALTDGAVTTDNEASPSSMPDGTPPPQEAEE	2	127	157	0	1
DALTDGAVTTDNEASPSSMPDGTPPPQEAEEPSL	3	127	160	1	3
DALTDGAVTTDNEASPSSMPDGTPP PQEAEEPSLLKKLLLAPANTQL	3	127	173	0	2
AVTTDNEASPSSMPDGTPPPQE	2	133	154	2	1
AEEPSL	1	155	160	0	2
AEEPSLLKKLLL	3	155	166	−2	2
PSLLKKLLLAPANTQL	2	158	173	−1	3
PSLLKKLLLAPANTQL	3	158	173	0	4
LKKLLLAPA	2	161	169	0	3
LKKLLLAPAN	2	161	170	1	3
LKKLLLAPANTQ	2	161	172	−1	1
LKKLLLAPANTQL	1	161	173	−3	2
LKKLLLAPANTQL	2	161	173	−1	1
LKKLLLAPANTQL	3	161	173	−1	2
LKKLLLAPANTQLS	2	161	174	1	2
LKKLLLAPANTQLS	3	161	174	2	2
LKKLLLAPANTQLSY	2	161	175	0	1
LKKLLLAPANTQLSY	3	161	175	−1	2
KKLLLAPANTQL	2	162	173	−1	1
LLLAPANTQL	1	164	173	2	2
LLLAPANTQL	2	164	173	0	2
SYNECSG	1	174	180	2	2
SYNECSGL	2	174	181	1	5
SYNECSGLSTQNHAANHTHRIRTNPAI	3	174	200	2	5
LLKYLTTND	2	228	236	−3	2
LKYLTTND	1	229	236	−1	2
LKYLTTND	2	229	236	−2	2
LTTND	1	232	236	−4	12

Table S5. Comparison of the hydrodynamic parameters from shape reconstructions and experimentally determined values

	ERRγLBD	Binary complex
Sedimentation coefficient of SAXS reconstructed shape*	3.5	3.4
Sedimentation velocity analysis	3.8	3.95
R_s of SAXS reconstructed shape*	35.3 Å	50.6 Å
R_s from SEC analysis	33.2 Å	51.7 Å

*As calculated by HYDROPRO.